Detection of glioblastoma response to temozolomide combined with bevacizumab based on μMRI and μPET imaging reveals [^{18}F]-fluoro-L-thymidine as an early and robust predictive marker for treatment efficacy

Aurélien Corroyer-Dulmont, Elodie A. Pérès, Edwige Petit, Jean-Sébastien Guillamo, Nathalie Varoqueaux, Simon Roussel, Jérôme Toutain, Didier Divoux, Eric T. Mackenzie, Jérôme Delamare, et al.

Neuro-Oncology 15(1):41–56, 2013.
doi:10.1093/neuonc/nos260
Advance Access publication October 31, 2012

Detection of glioblastoma response to temozolomide combined with bevacizumab based on μMRI and μPET imaging reveals [^{18}F]-fluoro-L-thymidine as an early and robust predictive marker for treatment efficacy

Aurélien Corroyer-Dulmont, Elodie A. Pérès, Edwige Petit, Jean-Sébastien Guillamo, Nathalie Varoqueaux, Simon Roussel, Jérôme Toutain, Didier Divoux, Eric T. MacKenzie, Jérôme Delamare, Méziane Ibazizène, Myriam Lecocq, Andréas H. Jacobs, Louisa Barré, Myriam Bernaudin, and Samuel Valable

CNRS, UMR ISTCT 6301, CERVOxy and LDM-TEP groups. GIP CYCERON, Bd Henri Becquerel, BP5229, 14074 CAEN cedex, France (A.C.-D., E.A.P., E.P., J.-S.G., S.R., J.T., D.D., E.T.M., J.D., M.I., M.L., L.B., M.B., S.V.); Université de Caen Basse-Normandie, UMR ISTCT 6301, CERVOxy and LDM-TEP groups. GIP CYCERON, Bd Henri Becquerel, BP5229, 14074 CAEN cedex, France (A.C.-D., E.A.P., E.P., J.-S.G., S.R., J.T., D.D., E.T.M., J.D., M.I., M.L., L.B., M.B., S.V.); CEA, DSV/I2BM, UMR ISTCT 6301, CERVOxy and LDM-TEP groups. GIP CYCERON, Bd Henri Becquerel, BP5229, 14074 CAEN cedex, France (A.C.-D., E.A.P., E.P., J.-S.G., S.R., J.T., D.D., E.T.M., J.D., M.I., M.L., L.B., M.B., S.V.); CHU de Caen, Service de Neurologie. Bd Côte de Nacre, Caen, France (J.-S.G.); Roche SAS, Neuilly sur Seine, France (N.V.); European Institute for Molecular Imaging (EIMI) at the Westphalian Wilhelms University (WWU), Münster, Germany (A.H.J.)

The individualized care of glioma patients ought to benefit from imaging biomarkers as precocious predictors of therapeutic efficacy. Contrast enhanced MRI and [^{18}F]-fluorodeoxyglucose (FDG)–PET are routinely used in clinical settings; their ability to forecast the therapeutic response is controversial. The objectives of our preclinical study were to analyze sensitive μMRI and/or μPET imaging biomarkers to predict the efficacy of anti-angiogenic and/or chemotherapeutic regimens. Human U87 and U251 orthotopic glioma models were implanted in nude rats. Temozolomide and/or bevacizumab were administered. μMRI (anatomical, diffusion, and microrheological parameters) and μPET ([^{18}F]-FDG and [^{18}F]-fluoro-L-thymidine [FLT]–PET) studies were undertaken soon (t_1) after treatment initiation compared with late anatomical μMRI evaluation of tumor volume (t_2) and overall survival. In both models, FDG and FLT uptakes were attenuated at t_1 in response to temozolomide alone or with bevacizumab. The distribution of FLT, reflecting intratumoral heterogeneity, was also modified. FDG was less predictive for treatment efficacy than was FLT (also highly correlated with outcome, $P < .001$ for both models). Cerebral blood volume was significantly decreased by temozolomide + bevacizumab and was correlated with survival for rats with U87 implants. While FLT was highly predictive of treatment efficacy, a combination of imaging biomarkers was superior to any one alone ($P < .0001$ in both tumors with outcome). Our results indicate that FLT is a sensitive predictor of treatment efficacy and that predictability is enhanced by a combination of imaging biomarkers. These findings may translate clinically in that individualized glioma treatments could be decided in given patients after PET/MRI examinations.

Received July 24, 2012; accepted August 27, 2012.

Corresponding author: Dr. Samuel Valable, UMR 6301-ISTCT, CERVOxy group, GIP CYCERON, Bd Henri Becquerel, BP5229, 14074 CAEN cedex, France (valable@cyceron.fr).

Keywords: anti-angiogenic, chemotherapy, FLT-PET, glioma, MRI.

Glioblastoma multiforme (GBM) is the most frequent primary malignant brain tumor in adults, with a highly deleterious disease course. Treatment of patients with GBM is based on a multidisciplinary approach that includes surgery and fractionated radio- and chemotherapy, as well as recent targeted therapies.[1] However, despite a combination of temozolomide (TMZ) with radiotherapy, median survival is still limited to about 15 months from time of diagnosis,[2] and the efficacy of current treatment strategies needs further improvement.

GBM is manifested as densely vascularized brain tumors, and, therefore, targeted anti-angiogenic therapies show promise as additional treatment paradigms.[3] To date, anti-angiogenic therapies based on the inhibition of vascular endothelial growth factor (VEGF) and VEGF receptor signaling are reported as being the most effective strategies.[4] For instance, bevacizumab, a humanized monoclonal antibody raised against VEGF, has shown encouraging results in patients with recurrent GBM.[5] Besides their direct effects on tumor vessels, anti-angiogenic therapies could also increase the efficacy of chemotherapeutic strategies either alone[6,7] or in combination with irradiation.[8]

To quantitatively follow the response of gliomas to therapy, various geometric criteria based on CT, MRI, and [^{18}F]-fluorodeoxyglucose (FDG)–PET[9] imaging have been proposed and considered as standard for clinical investigations. However, the widespread use of targeted therapies such as anti-angiogenic molecules either in combination with chemotherapy[7] or irradiation[8] or as stand-alone intervention has indicated limitations of these criteria, such as, for instance, "pseudoresponse"[10] and "pseudoprogression."[11]

Accordingly, the prediction of efficacy of innovative anticancer treatments awaits the development and/or the identification of novel imaging biomarkers. Modern advances in neuroimaging techniques such as MRI and PET should help to define surrogate imaging biomarkers[12] with respect to their ability (i) to noninvasively detect functional and metabolic changes, (ii) to take into account the spatial heterogeneity and textural features within the tumor mass, and (iii) to allow characterization of tumor cells and vasculature. In addition to MRI-based standard radiographic assessments, diffusion imaging[13–15] as well as the characterization of various microrheological parameters[16,17] have been suggested to be of interest to assess tumor response to chemo- and/or radiotherapies as well as anti-angiogenic approaches.

With PET, alongside FDG, numerous more targeted radiotracers have been developed (see Dhermain et al[12] and Wester[18]) to quantify cell proliferation by 3′-[^{18}F]fluoro-3′-deoxy-L-thymidine (FLT)[19] or amino acid metabolism by *o*-(2-[^{18}F]fluoroethyl)-L-tyrosine[20] or methyl-[^{11}C]-L-methionine.[21] These radiotracers are of interest to evaluate the response of patients with gliomas subjected to radio- or chemotherapy.

As gliomas are highly dynamic and heterogeneous disease entities, many patients with a glioma may benefit from combined and sequential therapies.[22] Therefore, a panel of various imaging biomarkers is of interest in the field of neuro-oncology and, more specifically, in the context of targeted therapies and decisions for personalized treatment.

Objectives

The aim of the present study was to analyze at the preclinical level the most sensitive and accurate imaging biomarkers capable of predicting therapeutic efficacy in experimental gliomas through a combination of an anti-angiogenic drug and a chemotherapeutic agent. To replicate the most salient aspects of human GBM we used 2 different human orthotopic brain tumors—known to exhibit different patterns in term of vasculature, invasion, and proliferation—growing in immunodeficient rats treated with TMZ, bevacizumab, or both. Functional and metabolic μMRI as well as μPET were performed early after the initiation of the treatment in order to discriminate predictive imaging biomarkers of treatment efficacy as assessed by the analysis of animal survival. Of the various MRI parameters, we focused on T2-weighted (T2w) hyperintensity volumes, diffusion, indices of perfusion, cerebral blood volume (CBV), vessel size index (VSI), and vascular permeability. For μPET biomarkers, we focused on glucose metabolism and cell proliferation through the use of FDG and FLT. To go further in the interpretation of FLT uptake, we also analyzed the heterogeneity in the images.[23]

Finally, we estimated the added diagnostic value of the combination of multimodal imaging biomarkers derived from multimodal imaging as sensitive and selective predictors of treatment efficacy.

Material and Methods

Cell Cultures, Rat Glioma Models, and Treatments

Human U87 (U87-MG for malignant glioma; American Type Culture Collection HTB-14) and human U251 glioma (National Cancer Institute) cells were grown in Dulbecco's modified Eagle's medium 1 g/L of glucose supplemented with 2 mM glutamine (Sigma-Aldrich) and 10% fetal calf serum (Invitrogen).

The animal investigations were performed under the European directive (86/609/EC) as enacted in national legislation. The license to investigate was given to S.V. (14–55) in authorized housing and laboratories (B14118001) and with the permission of the regional committee on animal ethics (CENOMEXA [Comité d'Ethique Normandie en Matière d'Expérimentation Animale], 0611-02). The rats were maintained in specific pathogen-free housing and were fed γ-irradiated laboratory chow and water ad libitum.

Animals were manipulated under deep anesthesia (5% isoflurane for induction, 2% for maintenance in 70% N_2O/30% O_2). Body temperature was monitored and maintained at 37.5 ± 0.5°C throughout the experiments by a rectal probe connected to an electric blanket.

Nude athymic rats (200–250 g; Charles River Laboratory for the U87 cell line, Harlan Laboratories for the U251 cell line) were placed on a stereotactic head holder, and a scalp incision was performed along the sagittal suture. A 1-mm diameter burr hole was drilled in the skull, 3 mm lateral to the bregma. U87 and U251 cells (5.10^4 cells in 3 μL phosphate buffered saline [PBS]–glutamine 2 mM) were injected over 6 min via a fine needle (30 G) connected to a Hamilton syringe.[24] The injection site was the right caudate-putamen, at a depth of 6 mm beneath the calvarium. The needle was removed slowly 5 min after the end of the injection, and the burr hole was sealed with dental cement. Eight animals per group were allocated for all imaging studies, and 3 additional rats were autopsied at the time of the last PET imaging for neurohistological analyses.

Bevacizumab (Avastin, Roche) was administered intraperitoneally (10 mg/kg in saline),[25] and TMZ (40 mg/kg in saline) was given per os for both models when glioma had reached a volume of about 20 mm^3 as depicted by MRI. Control animals received saline both i.p. and per os. The detailed schedule of the treatments and imaging is illustrated in Fig. 1.

Micro MRI

For all imaging experiments, the rat was in pronation, its head secured via ear and tooth bars. Respiration was monitored by a pressure-sensitive balloon adhered to the abdomen. μMRI was performed on a 7-tesla horizontal magnet (Pharmascan, Bruker). A cross coil configuration was used (volume/surface coil). For subsequent slice positioning, we performed rapid imaging (fast low angle shot sequence; repetition time (TR)/echo time (TE) = 100/4 ms; resolution 0.39 × 0.39 × 3 mm^3, acquisition time = 12 s) .

Tumor-associated edema was detected using a T2w sequence (RARE [rapid acquisition with refocused echoes]; acceleration factor, 8; TR/effective TE = 5000/62.5 ms; number of experiments (NEX) = 1; 20 contiguous slices; resolution = 0.15 × 0.15 × 0.75 mm^3; acquisition time = 2 min).

All echo planar images (EPIs) were acquired with a single-shot, motion artifact and ghost-free, double-sampling k-space coverage with identical bandwidth and geometry (10 contiguous slices, resolution = 0.3 × 0.3 × 1.5 mm^3) with saturation slices at the edges of the field of view. The apparent diffusion coefficient (ADC) of water was computed from diffusion-weighted spin-echo EPIs (30 diffusion directions; TR/TE = 3000/46.3 ms; NEX = 1, acquisition time = 3 min 30 s) with $b = 1000$ s mm^{-2} and 5 reference images ($b \approx 0$ s mm^{-2}).

Cerebrovascular parameters were measured once at 5 days after the treatment (see Fig. 1). Prior to injection of the contrast agents, T2*w (TR/TE = 20 000/12.0 ms, NEX = 3) and T2w (TR/TE = 20 000/80 ms, NEX = 3) EPIs were acquired. Inversion-recovery EPIs were acquired to compute T1 maps (TR/TE = 10 250/7.443 ms; 15 inversion times, range 37.8–4937.8 ms; NEX = 1; acquisition time = 1 min 42 s).

Dynamic susceptibility contrast MRI.—Gradient echo EPIs were acquired for 15 s before and 105 s after a bolus injection of particles of iron oxide (66 μmol kg^{-1}, P904)[26] (TR/effective TE = 400/9.17 ms; number of repetitions = 300; 10 slices; acquisition time = 2 min).

Imaging of fractional (f)CBV and VSI.—Immediately thereafter, a second administration of P904 was realized to achieve a total dose of 200 μmol kg^{-1}, and single-shot T2*w and T2w EPIs were acquired.

Dynamic T1 maps.—Three T1 maps were then acquired prior to injection of gadolinium–tetraazacyclododecane tetraacetic acid (Gd-DOTA; 200 μmol kg^{-1}; Dotarem), followed by 5 consecutive T1 maps.

Micro PET

[^{18}F]-FDG was produced by Cyclopharma; [^{18}F]-FLT was furnished by the Laboratoire de Développement Méthodologique en TEP as previously described.[19] Images were acquired on a μPET Siemens Inveon preclinical system on 2 consecutive days (see Fig. 1). An

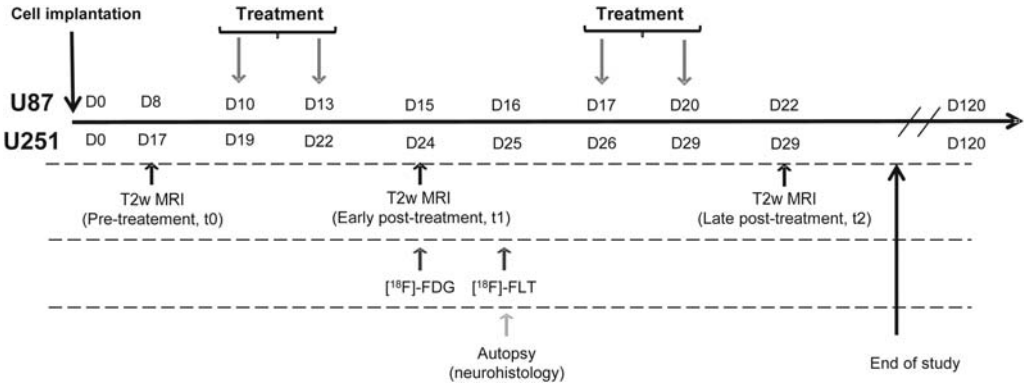

Fig. 1. Experimental paradigm and outline employing human U87 and U251 glioma models in conjunction with μMRI and μPET.

x-ray scan was employed to generate attenuation maps just prior to an emission scan of 20 min initiated 60 min (FDG, 66 MBq kg^{-1}) and 40 min (FLT, 66 MBq kg^{-1}) after the injection, in the caudal vein, of the radiotracer. All images were reconstructed by the iterative ordered-subset expectation maximization 2D algorithm.

Image Processing and Analysis

Image analysis was performed with in-house macros based on ImageJ software (http://rsb.info.nih.gov/ij/, 1997–2009). μPET analyses were performed by PMOD 3.1.[27]

MRI tumor volume.—Tumor delineation was performed manually on all adjacent T2w slices. Tumor volume was achieved by multiplication of the tumor surfaces by the slice thickness. The region of interest (ROI) corresponding to the tumor or to the healthy contralateral tissue was used thereafter for all other parameters.

Vascular parameters.—Indices of perfusion were obtained from the first pass of P904. Maps of fCBV (expressed as percent) and of VSI (expressed in micrometers) were computed from $\Delta R2^*$, $\Delta R2$ maps, ADC maps, and $\Delta\chi$, as shown in the following equations:

$$fCBV = \frac{3}{4\pi}\left(\frac{\Delta R2^*}{\gamma.\Delta\chi.B_0}\right) \quad (1)$$

$$VSI = 0.424\left(\frac{ADC}{\gamma.\Delta\chi.B_0}\right)^{1/2}\left(\frac{\Delta R_2^*}{\Delta R_2}\right)^{3/2} \quad (2)$$

where $\Delta\chi$ is the increase in the magnetic susceptibility difference between the extra- and intravascular compartments (nonrationalized units) induced by the presence of the contrast agent in the vasculature; B_0 is the main magnetic field (T); and γ is the gyromagnetic ratio of protons. Within each ROI and each map, voxels for which no reliable analysis could be performed were omitted (eg, fCBV values outside the range of validity of the method, ie, fCBV > 20%].[16]

Permeability was studied on dynamic T1 maps that were converted to gadolinium concentration maps, expressed in millimoles in equation 3,[28] where $r1$ is the relaxivity of Dotarem (2.6 $mM^{-1}\,s^{-1}$ at 7 teslas), and $T1$ corresponds to T1 measured prior to the administration of the contrast agent:

$$[Gd] = \frac{1}{r1}\left(\frac{1}{T1} - \frac{1}{T1_0}\right) \quad (3)$$

μMRI/μPET co-registration.—All μMRI experiments were executed such that all MRI parameters were anatomically registered to each other. A first automatic registration (PMOD 3.1) was performed between T2w MRI (reference) and the x-ray scan (input) by normalized mutual information algorithms, with the transformation matrix being applied to the corresponding emission scans. When necessary, the registration was manually refined. As a second step, μPET parameters were coregistered to μMRI parameters.

μPET analyses.—ROIs defined on T2w MRI were transferred onto all μPET images. To quantify FDG and FLT uptake, the measured tissue activity concentration (counts [kBq]/mL^{-1}) was divided by the injected activity, in kilobecquerels per gram of body weight (kBq/g^{-1}), to give a standardized uptake value (SUV; g/mL^{-1}).

Statistical Analyses

All data are presented as mean ± SD. Statistical analyses were obtained with JMP programs (SAS Institute). The different tests used are detailed in each figure legend. Receiver-operating-characteristics curves were generated with JMP programs. The combination of imaging biomarkers was computed from general linear models with a JMP program. No outliers were removed from any set of data.

Immunohistochemistry

At the time of the last μPET session, 3 anesthetized rats were euthanized and their brains were removed, immediately snap frozen, and stored at −80°C. Coronal sections (20 μm) were cut on a cryostat. Immunohistochemical staining for rat endothelial cell antigen (RECA; 0.4 μg/mL; Abcam) and Ki67 (0.35 μg/mL, MIB-1; Dako) were used to characterize glioma vascularization and proliferation, respectively. After blocking nonspecific binding in bovine serum albumin (BSA) 3%–PBS-Triton X100 0.3% for 1 h at room temperature, slices were incubated overnight with antibodies at 4°C in 1% BSA-PBS-Triton X100 0.3%, and revelation was achieved by Cy3-linked goat antimouse immunoglobulin G (1 μg/mL; Jackson Immunoresearch). Nuclei were counterstained with Hoechst 33342 (Sigma-Aldrich). Tissue sections were examined at ×20 magnification for RECA and ×40 for Ki67 with a Leica DM6000 microscope. For Ki67 quantification, 4 slices per rat were used with 3 photographs per slice, and nuclei were counted automatically using ImageJ.

Survival Study

After imaging, we followed the rats, except those animals euthanized for immunohistochemistry, for a survival study. At the onset, we defined 110 days as an arbitrary end point for overall outcome survival.

Results

Effects of Each Treatment Regimen on Tumor Volumes and Survival

The representative T2w μMRIs for the tumor models and each of the 4 treatment groups are given (Fig. 2A and D) prior to treatment as well as 5 (early, t_1) and 12 or 10 (late, t_2) days after the initial administration of vehicle alone or TMZ, bevacizumab, and TMZ + bevacizumab.

In each GBM model, analyses of tumor volumes from early (t_1) T2w μMRI revealed no effects of bevacizumab alone (Fig. 2B and E), a slight decrease in tumor volume with TMZ alone in the U251 model but no effect in the U87 model, and a slight decrease in tumor volume with TMZ + bevacizumab in both models ($P < .05$ and $P < .01$ vs control group for U87-MG and U251 groups, respectively). However, the effect of treatment became more apparent on the later (t_2) μMRI analyses because TMZ alone or TMZ + bevacizumab significantly decreased the growth in tumor volume in both models ($P < .0001$ vs control and bevacizumab groups) (Fig. 2B and E). Bevacizumab alone had no statistically significant effects on tumor volume and induced an increase in survival for only the U87 model (log rank $P < .01$).

In both models, the attenuation of the expanding glioma, as observed on late (t_2) μMRI paralleled an increase in animal survival, with a highly significant effect ($P < .001$) of either TMZ alone or TMZ + bevacizumab (Fig. 2C and F).

Early Assessment of Response to Treatment with MRI Biomarkers

Diffusion of water molecules.—ADC maps were used as indices of cell density and viability. From ADC maps, the U87 tumor was nearly indistinguishable relative to the healthy contralateral caudate-putamen (contralateral $= 804 \pm 66\ \mu m^2\ s^{-1}$, control tumor $= 810 \pm 49\ \mu m^2\ s^{-1}$), and no treatment effects were observed with the measurement of ADC values (bevacizumab $= 876 \pm 99\ \mu m^2\ s^{-1}$, TMZ $= 917 \pm 41\ \mu m^2\ s^{-1}$, TMZ + bevacizumab $= 879 \pm 85\ \mu m^2\ s^{-1}$).

The U251 model was characterized by a slight but nonsignificant increase in ADC values compared with the contralateral tissue (contralateral $= 826 \pm 66\ \mu m^2\ s^{-1}$, control tumor $= 877 \pm 63\ \mu m^2\ s^{-1}$). No changes in ADC values were observed in the treatment groups (bevacizumab $= 833 \pm 114\ \mu m^2\ s^{-1}$, TMZ $= 922 \pm 152\ \mu m^2\ s^{-1}$, TMZ + bevacizumab $= 832 \pm 88\ \mu m^2\ s^{-1}$).

Cerebrovascular Parameters

We initially analyzed the first-pass kinetics of the particles of iron oxide as indices of perfusion. In the U87-implanted rats, we observed a delay of time-to-peak in the tumors of the control group compared with healthy contralateral brain tissue (Fig. 3A) and an absence of a clear separation between the first pass and the subsequent recirculation of the contrast agent. There was no significant difference in these parameters between groups, which may reflect an absence of treatment effects on perfusion within the time frame studied (Fig. 3A). Of note is the absence of a return to baseline with respect to the high susceptibility effect of the particles of iron oxide.

Elevated fCBV was observed in the tumors of the control group compared with the contralateral side (relative [r]CBV $= 2.20 \pm 0.63$, $P < .001$). Anti-angiogenic treatment alone had no effect on rCBV (2.12 ± 0.37), but the administration of TMZ alone or in combination with bevacizumab significantly decreased rCBV compared with the control group (1.72 ± 0.31 and 1.47 ± 0.27, respectively; $P < .05$ for TMZ alone and $P < .01$ for TMZ + bevacizumab vs control group) (Fig. 3B).

RECA immunostaining failed to reveal any major treatment effects on vasculature for this model (Fig. 4A), but all treatment groups demonstrated obvious differences compared with healthy contralateral tissue.

In the U251 model, the signal shape of the first-pass kinetics of iron oxide was identical—irrespective of the treatment—and was close to that observed in healthy contralateral brain tissue, with subsequent passes of the contrast agent being more apparent than in the U87 model (Fig. 3A and C). We observed an elevated fCBV in the tumors of the control group and the TMZ group and a slight but nonsignificant decrease in fCBV in the bevacizumab and TMZ + bevacizumab groups compared with the control group ($P = .07$ and $P = .06$ for bevacizumab and TMZ + bevacizumab, respectively) (Fig. 3D).

Based on RECA immunostaining, neovascularization in the U251 model was less proliferative than in the U87 model. A decrease in vessel density was observed in the bevacizumab and TMZ + bevacizumab groups compared with the control and TMZ groups (Fig. 4A).

Based on the known characteristics of the neoplastic vasculature, vessels in both glioma models were highly permeable to Gd-DOTA (Supplementary data). Vessels of the TMZ group were significantly ($P < .05$) more permeable than those of the bevacizumab group for the U87 model. With its known antipermeability effects, the presence of bevacizumab either alone or in combination with TMZ decreased the leakage of the contrast agent in the U251 model.

Early Assessment of Treatment Response with μPET Biomarkers

As would be expected, the gliomas of the control groups were characterized by an increased uptake of FDG and FLT compared with healthy tissues (Fig. 5A and E). In the U87 model, FDG uptake was significantly decreased in the TMZ + bevacizumab group compared with the control group (Fig. 5A and B). In addition, FLT uptake was significantly decreased not only in the TMZ + bevacizumab group but also in the TMZ group compared

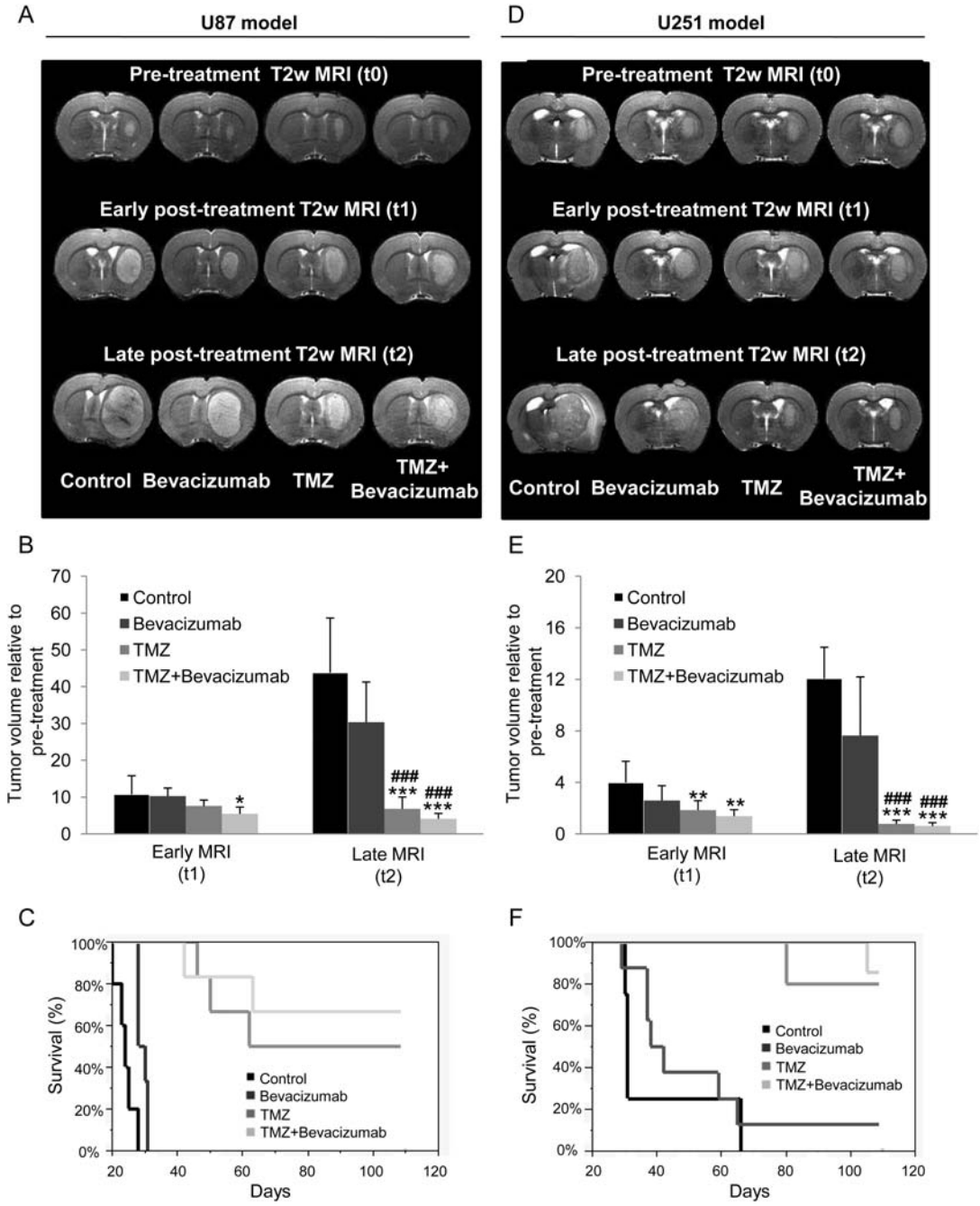

Fig. 2. Determination of treatment effects on tumor volume and survival. (A–D) Representative T2w MRIs for the 4 different groups of animals (control, bevacizumab, TMZ, TMZ + bevacizumab) before, early (t_1, 5 days), and late (t_2, 12 days) after initiation of the treatments for the U87 (A) and the U251 (D) models. (B–E) Quantitative tumor volume analyses at early and late times after initiation of the treatments for the U87 (B) and the U251 (E) model. U87 model: mean ± SD, $n = 6$ for all groups except control ($n = 7$). U251 model: mean ± SD, $n = 8$ for bevacizumab and TMZ groups, $n = 7$ for TMZ + bevacizumab group, and $n = 5$ for control group. $^{*}P < .05$ vs control group at respective time, $^{**}P < .01$ vs control group at respective time, $^{***}P < .001$ vs control group at respective time, $^{\#\#\#}P < .001$ vs bevacizumab group at respective time with a 1-way analysis of variance and Tukey's post hoc test. (C–F) Kaplan–Meier curves of survival for the U87 (C) and the U251 (F) model.

with the control and bevacizumab groups (Fig. 5A and C). FLT was markedly more sensitive than FDG to the effects of treatment. $P = .012$ for FDG in the TMZ + bevacizumab group, and $P < .0001$ for FLT in the same group.

The results obtained by FLT-μPET accord with the quantification of the immunohistochemical staining for Ki67 (Fig. 4B). Indeed, no effect of bevacizumab was observed, but chemotherapeutic treatment alone and in combination with bevacizumab significantly reduced

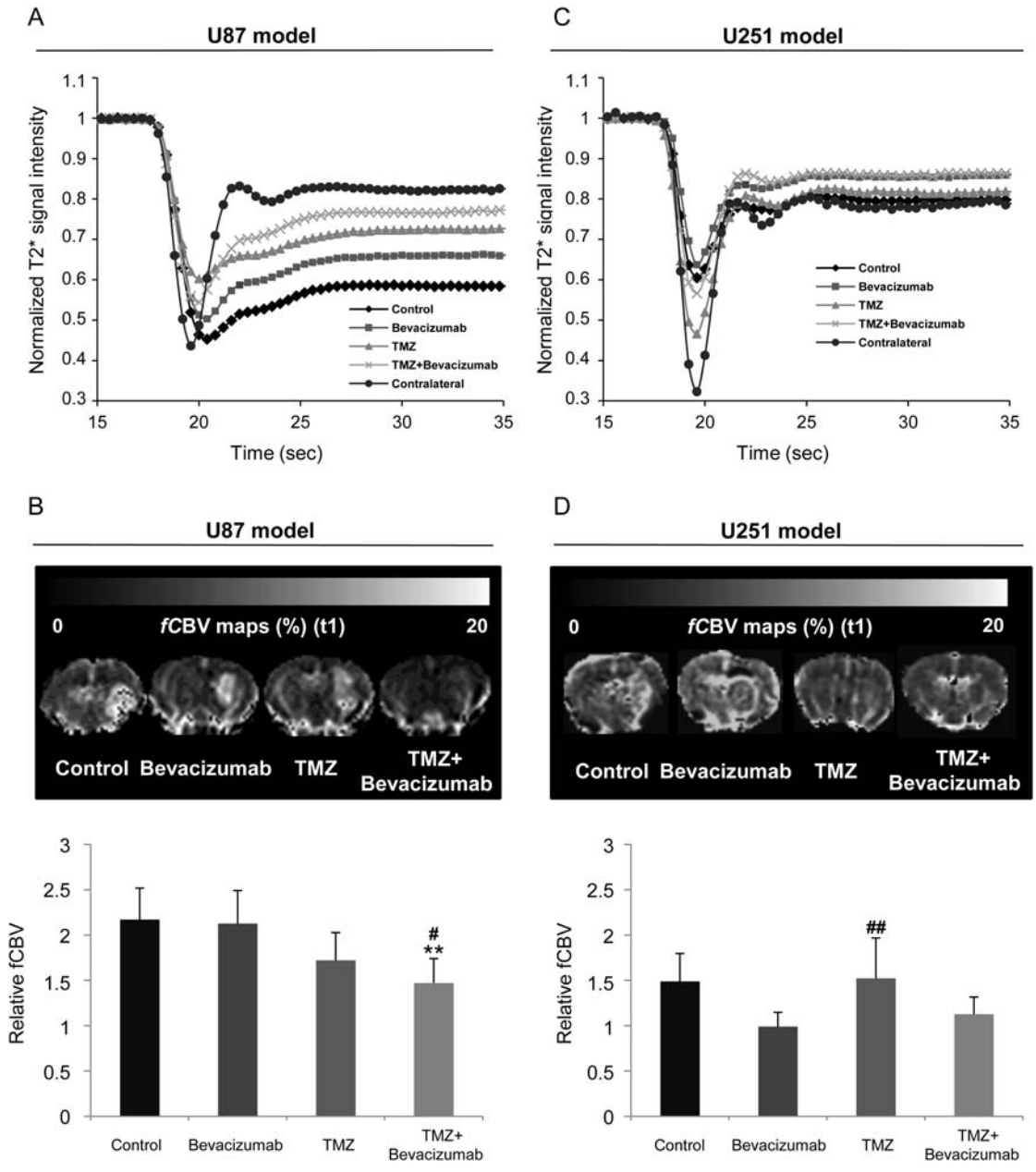

Fig. 3. Early MRI determination of treatment effects on vascular measures. (A–C) Average signal of dynamic susceptibility contrast MRI over 35 s before and after a bolus injection of P904(r) in healthy contralateral caudate-putamen and in the tumor of the 4 different groups of animals for the U87 (A) and U251 (C) models. (B–D) Representative maps and corresponding quantitative analyses of fCBV for the U87 (A) and U251 (C) models. U87 model: mean ± SD, $n = 6$ for all groups except control ($n = 7$). U251 model: mean ± SD, $n = 8$ for bevacizumab and TMZ groups, $n = 7$ for TMZ + bevacizumab group, and $n = 5$ for control group. *$P < .05$, **$P < .01$ vs control group, and #$P < .05$ vs bevacizumab group with a 1-way analysis of variance and Tukey's post hoc test.

the number of Ki67-positive cells in the U87 model (control = 1468 ± 87 cells/mm^2; bevacizumab = 1457 ± 273 cells/mm^2; TMZ = 407 ± 92 cells/mm^2; $P < .001$ vs control and bevacizumab groups); TMZ + bevacizumab = 677 ± 202 cells/mm^2 ($P < .01$ vs control and bevacizumab groups).

Apparent to the naked eyed, the FLT uptake was highly variable within the tumor, a heterogeneity that was attenuated by TMZ or TMZ + bevacizumab. To evaluate this observation, we generated histograms of the distribution of FLT (Fig. 5D) and subsequently analyzed various indices of population heterogeneity and texture (summarized in Table 2). In parallel to a decrease in both mean and median FLT uptake in the presence of TMZ alone or in combination with bevacizumab, the range and the SD were reduced, and kurtosis and

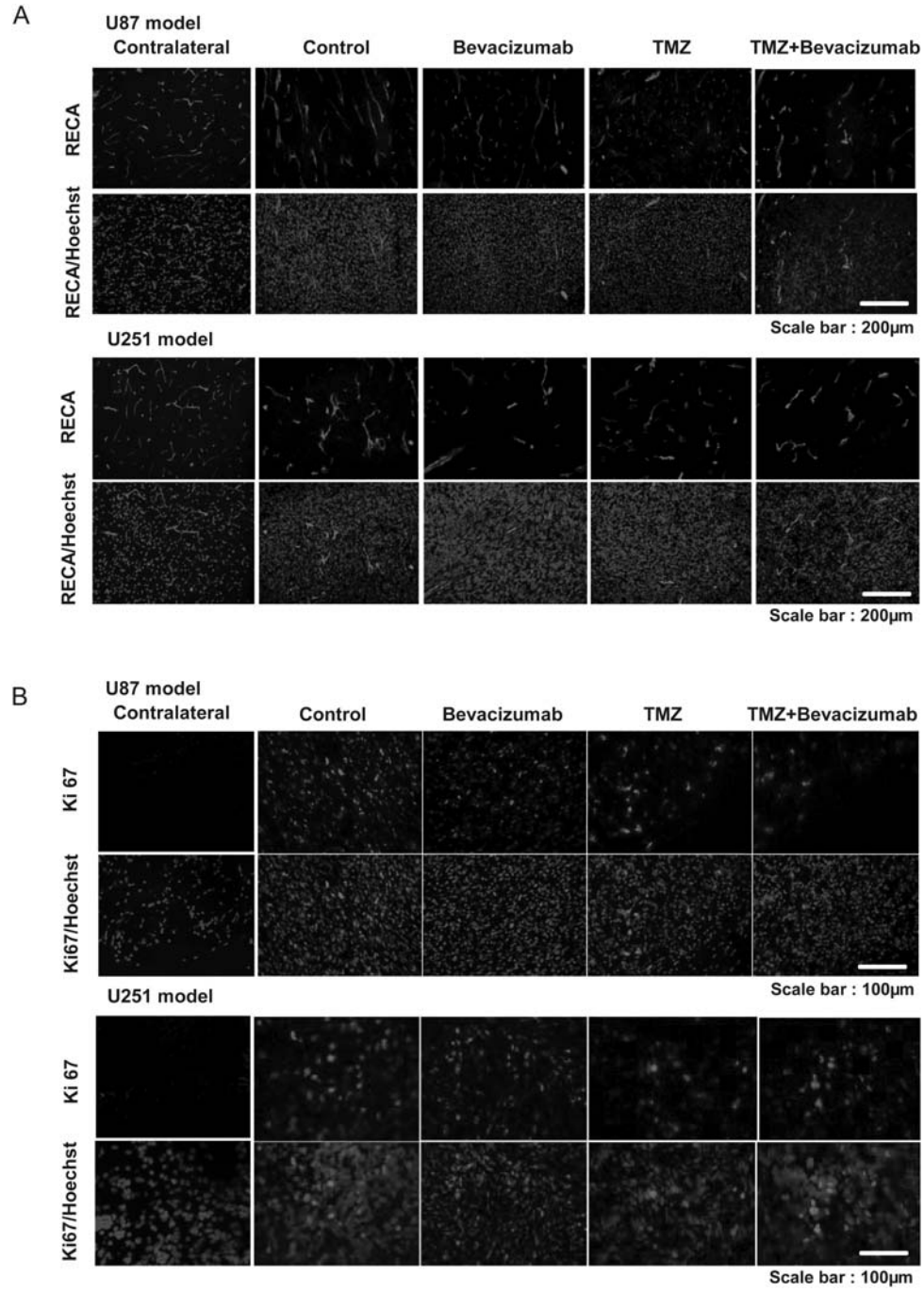

Fig. 4. Early immunohistochemical determination of treatment effects on tumor vasculature and cell proliferation. (A) Representative images of RECA immunostaining (red) of 1 rat in each of the 4 different groups with Hoechst 33342 counterstaining (blue) for the U87 and U251 models. Scale bar = 200 μm. (B) Representative images of Ki67 immunostaining (red) of 1 rat in each of the 4 different groups with Hoechst 33342 counterstaining (blue) for the U87 (A) and U251 (B) models. Scale bar = 100 μm.

skewness were significantly increased compared with the control and bevacizumab groups.

As with the U87 model, in the U251 model we observed a decrease in FDG uptake for the bevacizumab and TMZ groups ($P < .05$) and a similar but insignificant decrease in FDG uptake for the TMZ + bevacizumab group compared with the control group ($P = .058$)(Fig. 5E and F). Likewise, the index of proliferation, evaluated by FLT uptake, was significantly decreased in the presence of TMZ with bevacizumab ($P < .05$)(Fig. 5E and G).

These results are in accord with the quantification of immunohistochemical staining for Ki67 (Fig. 4B). No effect of bevacizumab was observed, but TMZ alone and in combination with bevacizumab significantly reduced the number of Ki67-positive cells

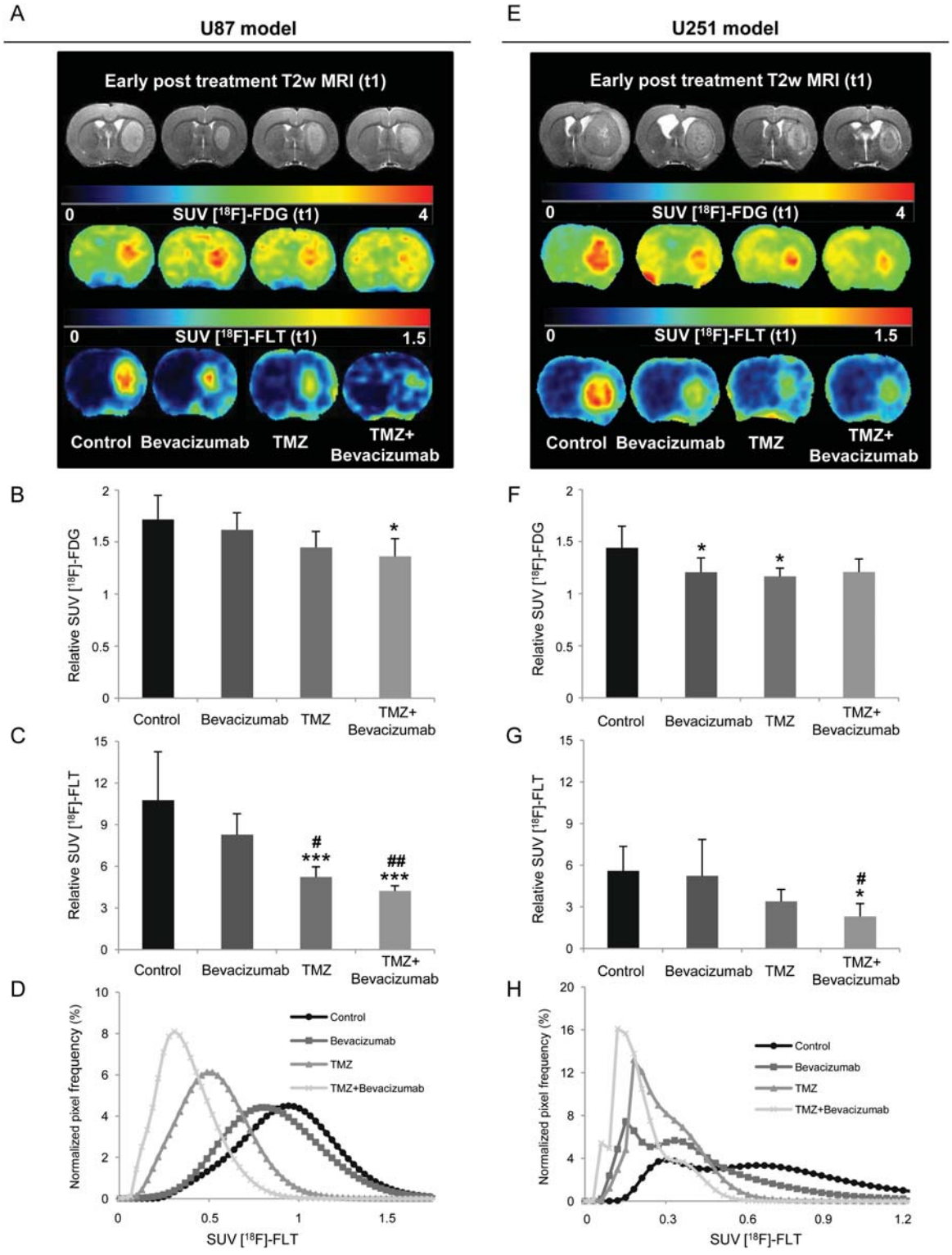

Fig. 5. Early PET determination of treatment effects on glucose metabolism and cell proliferation. (A–E) Representative images of FDG and FLT uptake for the 4 different groups of animals for the U87 (A) and U251 (E) models. (B–F) Quantitative relative FDG–SUV uptake (relative to contralateral uptake) for the U87 (B) and U251 (F) models. (C–G) Quantitative relative FLT–SUV (relative to contralateral uptake) for U87 (C) and U251 (G) tumors. U87 model: mean ± SD, $n = 6$ for all groups except control ($n = 7$). U251 model: mean ± SD, $n = 8$ for bevacizumab and TMZ groups, $n = 7$ for TMZ + bevacizumab group, and $n = 5$ for control group.*$P < .05$ vs control group. *$P < .05$ vs control group, **$P < .01$ vs control group, ***$P < .001$ vs control group, and #$P < .05$ vs bevacizumab group. ##$P < .01$ vs bevacizumab group, ###$P < .001$ vs bevacizumab group with a 1-way analysis of variance and Tukey's post hoc test. (D–H) Normalized FLT–SUV distribution histograms. Each histogram represents the mean histogram of all animals of each treatment group for the U87 (D) and U251 (H) models.

(control = 1925 ± 536 cells/mm^2; bevacizumab = 1656 ± 558 cells/mm^2; TMZ = 1101 ± 7 cells/mm^2; TMZ + bevacizumab = 1164 ± 173 cells/mm^2 [$P < .05$ vs control group]).

The untreated U251 rats displayed an abnormal frequency distribution of SUV parameters with FLT (Fig. 5F and Table 2), a type of population that may evoke the bimodal distribution identified elsewhere in GBM.[29] Similar nonnormal patterns of frequency distribution curves were seen in the 3 groups of treated rats but with significant changes in the median for the bevacizumab and TMZ groups and in the median, SD, kurtosis, and skewness in the TMZ + bevacizumab group compared with the control group.

Table 1. Correlations between biomarkers (or the combination of biomarkers) and overall survival

Imaging Biomarker	R^2	*P* Value
A U87 model		
T2w MRI, t_2	0.57	<.0001
[^{18}F]-FLT	0.42	.0007
[^{18}F]-FDG	0.38	.0016
CBV	0.28	.009
T2w MRI, t_1	0.20	.03
ADC	0.19	.03
VSI	0.0081	NS
C U251 model		
[^{18}F]-FLT	0.55	<.0001
T2w MRI, t_2	0.48	.0003
VSI	0.26	.01
T2w MRI, t_1	0.25	.01
[^{18}F]-FDG	0.09	NS
CBV	0.02	NS
ADC	0.0008	NS
B U87 model		
[^{18}F]-FLT*[^{18}F]-FDG	0.57	<.0001
[^{18}F]-FLT*CBV	0.49	.0002
[^{18}F]-FLT*CBV*[^{18}F]-FDG	0.64	<.0001
D U251 model		
[^{18}F]-FLT*[^{18}F]-FDG	0.67	<.0001
[^{18}F]-FLT*VSI	0.63	<.0001
[^{18}F]-FLT*VSI*[^{18}F]-FDG	0.68	<.0001

Correlation coefficient (R_2) and the corresponding *P* value between each imaging biomarker (A–C) or the combination of imaging biomarkers (B–D) with overall survival for the U87 (A–B) and U251 models (C–D).
Abbreviation: NS, not significant.

Predictive Value of Imaging Biomarkers

We then analyzed the capacity of imaging biomarkers to predict animal survival. The predictability of the biomarkers was assessed by the strength of the correlation (R^2) of the linear regression between survival time (with an imposed limit in our study) and the parameter under consideration (Table 1). Our results show that the most sensitive imaging biomarkers for MRI and PET were CBV and FLT for the U87 model (Table 1A) and VSI and FLT for the U251 model (Table 1C).

Various arguments speak in favor of FLT as a candidate for the early evaluation of treatment efficacy; in Fig. 6A and E, a representative animal is shown for the control and TMZ + bevacizumab groups at early (t_1) and late (t_2) times for MRI and t_1 for FLT for the U87 and U251 models, respectively. We observed a strong correlation between FLT uptake and the slope of tumor growth ($R^2 = 0.79$, $P < .0001$ and $R^2 = 0.33$, $P < .005$ for the U87 and U251 models, respectively) (Fig. 6B and F).

We also analyzed the relationships between [^{18}F]-FLT and survival. A highly significant correlation of a linear regression was obtained between [^{18}F]-FLT uptake and final outcome animal survival ($R^2 = 0.42$, $P < .001$ and $R^2 = 0.55$, $P < .0001$ for the U87 and U251 models, respectively) (Fig. 6C and G). Based on an FLT–SUV threshold derived from the area under the ROC curve, we showed that lesser [^{18}F]-FLT uptakes were associated with a significant increase in animal survival for both models (Fig. 6D and H), and in corollary, values greater than the ROC threshold indicated a gloomy prognosis.

Table 2. Analyses of distribution histograms of FLT–SUV

	Mean	Median	SD	Kurtosis	Skewness
A U87 model					
Control	0.93 (0.09)	0.90 (0.09)	0.24 (0.04)	0.68 (0.83)	1.44 (0.23)
Bevacizumab	0.83 (0.13)	0.82 (0.14)	0.24 (0.03)	0.62 (0.45)	1.44 (0.18)
TMZ	0.47 (0.12)***/###	0.46 (0.11)***/###	0.14 (0.04)**/##	4.17 (3.43)**	2.23 (0.58)*/#
TMZ + bevacizumab	0.36 (0.10)***/###	0.36 (0.10)***/###	0.12 (0.02)***/###	6.00 (4.43)**	2.63 (0.55)**/###
B U251 model					
Control	0.66 (0.45)	0.70 (0.35)	0.19 (0.11)	3.80 (4.27)	2.08 (0.93)
Bevacizumab	0.38 (0.25)	0.38 (0.18)*	0.11 (0.07)	12.28 (11.22)	3.30 (1.45)
TMZ	0.24 (0.13)#	0.27 (0.09)**	0.08 (0.03)	18.68 (17.28)	4.10 (1.52)
TMZ + bevacizumab	0.18 (0.11)*	0.21 (0.09)**	0.04 (0.01)*	35.66 (24.24)*	5.64 (1.81)**

Data represent the mean (SD) per group of the mean, median, SD, kurtosis, and skewness for each histogram of each animal. *$P < .05$ vs control group, **$P < .01$ vs control group, ***$P < .001$ vs control group, and #$P < .05$ vs bevacizumab group, ##$P < .01$ vs bevacizumab group, ###$P < .001$ vs bevacizumab group with a 1-way analysis of variance and Tukey's post hoc test.

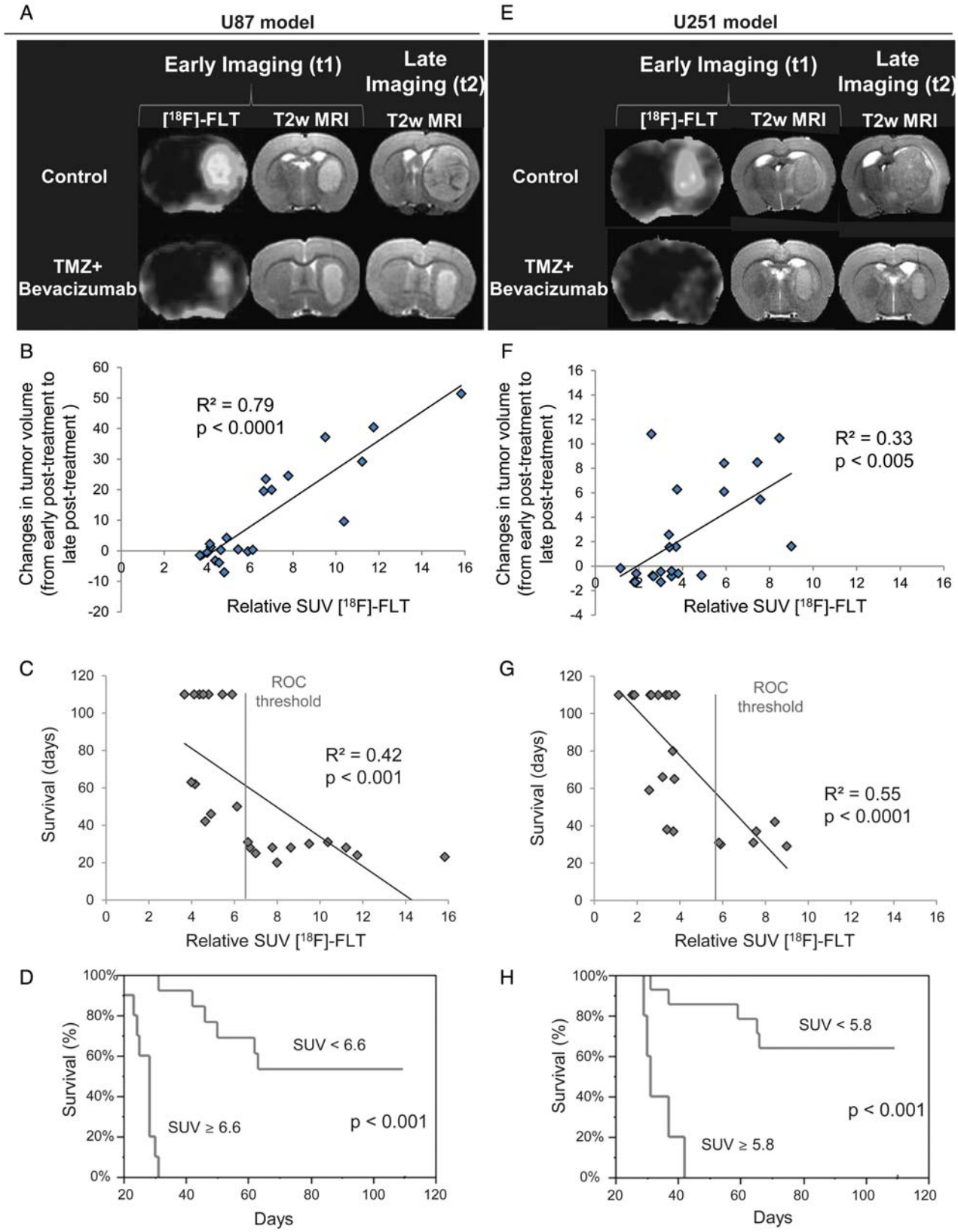

Fig. 6. Predictive value of imaging biomarkers. (A–E) Representative early FLT–SUV and T2w MRIs (t_1) with the corresponding late T2w MRI (t_2) for the U87 (A) and U251 (E) models. (B–F) Correlation graphs between relative FLT uptake and the slope of tumor volume evolution between early post-treatment (t_1) and late post-treatment (t_2) times (C) and between relative FLT uptake and overall survival (G) across models and treatments. (E–F) Kaplan–Meier survival curves for survival according to a cutoff value derived from the area under the ROC curve for FLT–SUV for U87 (E) and U251 (F) tumor types.

Predictive Value of Combinations of Imaging Biomarkers

The combination with FLT of the most predictive MRI biomarker (CBV for the U87 model and VSI for the U251 model) was correlated to animal survival (Table 1A and B). The strength of the correlation (R^2 and P value) was not higher than FLT alone for the U87 model (Fig. 7A) but rose to 0.67 (with $P < .0001$) for the U251 model (Fig. 7E). The combination of 1 MRI biomarker with FLT also allowed for discrimination of long-term survival from early death (Fig. 7B and F).

From Table 1B and D, we observe that a combination of 2 PET biomarkers with 1 MRI biomarker was the most predictive combination of imaging biomarkers, with an increase in the strength of R^2 to 0.68 ($P < .0001$) and 0.68 ($P < .0001$) for U87 and U251 models, respectively (Fig. 7C and G). These combinations were also of interest to discriminate long- and short-term outcome (Fig. 7D and H).

Discussion

In this study, we included 2 GBM types of different origin and distinct histological features.[30] The U87 model is rapidly expansive and portends early death; the U251 gliomas develop less rapidly but also have a bleak outcome. Both tumor types are highly amenable to treatment with TMZ, a potent alkylating agent. In contrast, bevacizumab was feeble in terms of overall outcome. A principal difficulty with our investigations was the remarkable potency of TMZ, which tended to divide the entire population into those who died early and those with excellent overall survival. Future protocols might consider intermediary doses of TMZ.

Our present results indicate that FLT-μPET serves as an imaging biomarker for the early prediction of the response to antiproliferative and/or anti-angiogenic treatment regimens in 2 distinct experimental human glioma models: biomarkers were measured against late tumor volumetry and overall survival. μMRI-based measures of tumor blood volume were less sensitive as predictors of a therapeutic response than FLT-μPET. In contrast, FDG-μPET was predictive in the U87-MG model but not in the U251 model. However, we also show that a combination of imaging biomarkers is strongly predictive of treatment efficacy (as determined by overall survival) for both models.

Patients with GBM benefit from a multidisciplinary treatment approach including surgery, radiotherapy, and chemotherapy with limited clinical efficacy. Additional and novel therapeutic approaches, such as the use of anti-angiogenic drugs, are attractive, especially in combination with antiproliferative agents.[31] The prospect of several future investigations also highlights the need for more robust and specific functional/molecular imaging parameters to enrich the present criteria of antitumoral efficiency that are based on simple structural or anatomical imaging. Indeed, anatomical imaging alone can lead to misinterpretation (pseudoresponse and pseudoprogression).[10,32] As with molecular and histological biomarkers, innovative functional/molecular imaging biomarkers will encourage the search for greater individualized therapies.[33,34]

When a vascular targeting molecule is associated with a cytotoxic treatment, it is of interest to focus not only on the vasculature but also on the tumor cells themselves. Our preclinical study shows that [^{18}F]-FLT PET and, to a lesser extent, CBV/μMRI or VSI/μMRI may be prognostic imaging biomarkers for early tumor response (in contradistinction to anatomical MRI) to a combinatory therapy aimed at both the vasculature and cancerous cells. Indeed, the correlation coefficients (R^2) between the early volume of the tumor, as measured by MRI, and overall survival were 0.20 and 0.25 in the U87 and U251 models, respectively. We observed that FDG was slightly correlated to survival in the U87 model ($R^2 = 0.38$, $P = .016$) but not in the U251 model ($R^2 = 0.09$, $P =$ NS). However, FLT, introduced over 10 years ago,[35] correlated intimately with overall survival for both tumor types ($R^2 = 0.42$ and 0.57; $P < .0001$ for U87 and U251 models, respectively). Our results are in line with those previously reported in ovarian cancer xenografts in which it was demonstrated that FLT uptake was markedly more sensitive than FDG[36] in the detection of the responses to Top216 chemotherapy. Our results also concur with those of Schwarzenberg and colleagues,[37] who recently demonstrated that FLT was more predictive than MRI of early treatment responses to recurrent glioma.

We analyzed the combination of imaging biomarkers. Although for the U87 model, the strength of the correlation was not increased, the fusion of 1 MRI biomarker and the PET biomarker increased the correlation between imaging biomarkers and animal survival. For both models, we noted that the association of 2 μPET biomarkers and 1 μMRI biomarker resulted in the highest correlation.

Overall, our data with those of others clearly indicate that FLT is a sensitive imaging biomarker and detects early responses to therapy (at least those induced by cytotoxic agents). The mean SUV as well as the textural distribution of FLT uptake were modified by the treatment. The nature and statistical analyses of FLT uptake are of considerable importance in the understanding of changes in tumor behavior after the initiation of therapy. For example, it has been shown recently that the heterogeneity of FDG uptake is predictive of response in esophageal tumors.[23]

FLT uptake can be analyzed by a classical 2-compartment model. It has been proposed that the enzymatic dissociation constant (Ki) should correlate more closely with cell proliferation than does SUV.[38] Although we conducted neither dynamic acquisitions nor compartmental analyses of FLT uptake, our SUV results were correlated with Ki-67 immunostaining and were also correlated with survival. It has also been suggested that the permeability of the blood–brain barrier (BBB) is a major modulator of FLT uptake.[39] In the present study, the permeability of the BBB was analyzed

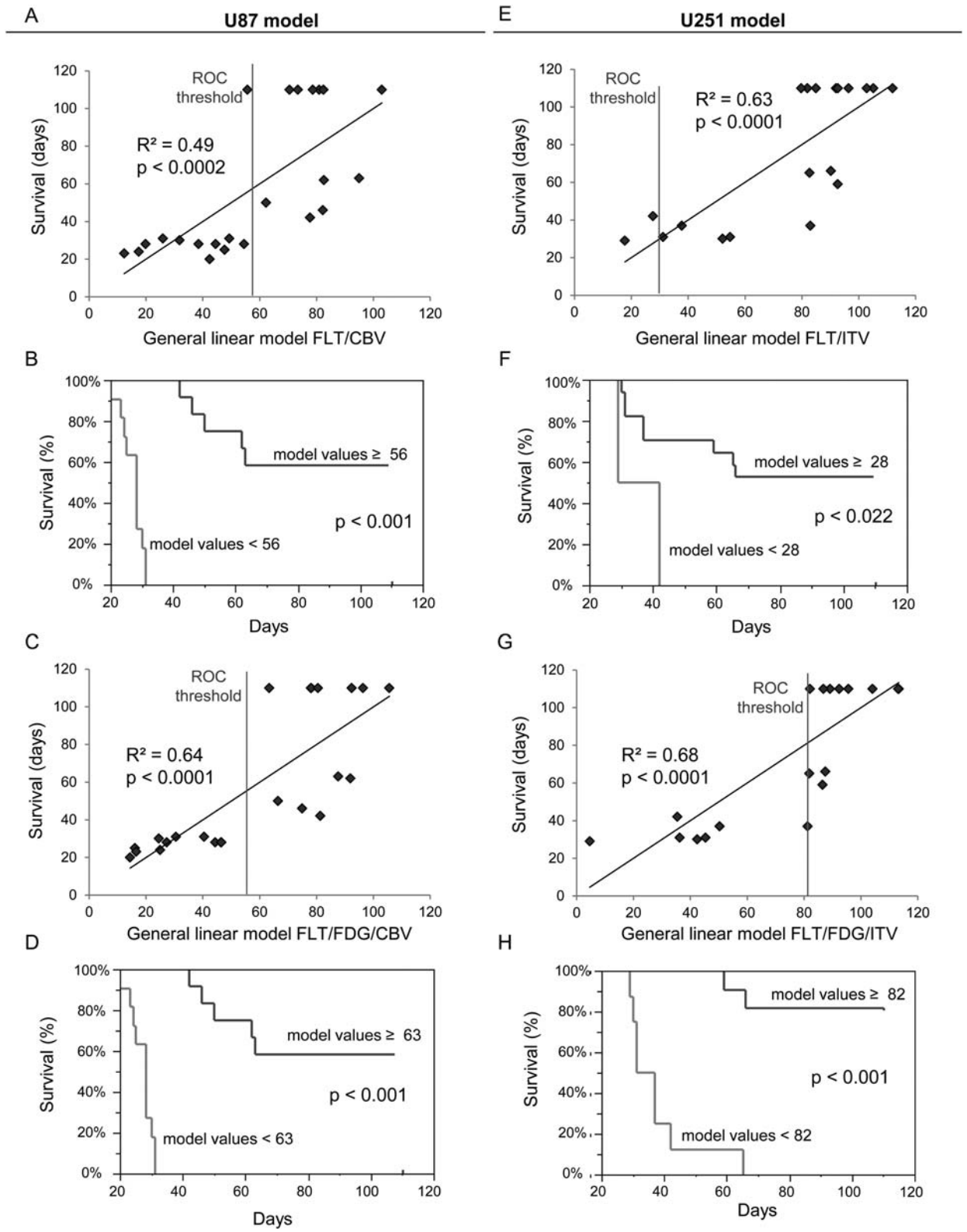

Fig. 7. Predictive value of a combination of imaging biomarkers. (A–E) Correlation graphs between a combination of FLT and CBV for the U87 model (A) and FLT and VSI for the U251 model (E) and overall survival. (B–F) Kaplan–Meier survival curves according to a cutoff value derived from the area under the ROC curve for the combination of FLT–SUV and CBV for the U87 model (B) or FLT–SUV and VSI CBV for the U87 model (F). (C–G) Correlations between a combination of overall survival and FLT, FDG, and CBV for the U87 model (C) and FLT, FDG, and VSI for the U251 model (G). (D–H) Kaplan–Meier survival curves according to a cutoff value derived from the area under the ROC curve for the combination of SUV–FLT/SUV–FDG/CBV for the U87 model (D) and FLT–SUV/FDG–SUV/VSI for the U251 (H) model.

dynamically using T1 mapping, and no correlation was observed between uptake of Gd-DOTA (≈700 Da) and uptake of FLT (≈300 Da) ($R^2 = 0.06$, $P > .05$ across models and treatments). For example, for the U87 model, we noted a marked decrease in FLT uptake in the rats treated with TMZ or TMZ + bevacizumab associated with an increase in BBB permeability to Gd-DOTA (see Supplementary data). Other arguments can be adduced. In focal cerebral ischemia, in which widespread edema and barrier disruption are signal features, FLT uptake was observed in a region where barrier disruption was not detected, thought to represent discrete neurogenesis.[40]

If mechanisms other than proliferation could not be excluded to influence the uptake of FLT, we found that FLT uptake could be used as a surrogate end point for overall survival.[41] Early enhanced FLT uptake was predictive of both late tumor volumes and overall survival ($R^2 = 0.71$, $P < .001$ across models and treatments). Our study also reinforces a pilot clinical study that showed that FLT uptake was more predictive of patient survival than was MRI volume in a cohort of GBM patients treated with a combination of bevacizumab and irinotecan.[42] Regardless of the nature of the treatment, it is interesting to note that relative FLT–SUV observed for the U87 and U251 control groups was inversely correlated to median survival (rFLT–SUV $= 11 \pm 3$ g /mL^{-1} for U87, median survival time = 24 days; rFLT–SUV $= 6 \pm 1$ g/mL^{-1} for U251, median survival time = 39 days).

Within the vasculature of the glioma, we noted that the indices of perfusion, derived from first-pass studies, were insensitive to treatment effects. Although both tumor models exhibited different temporal characteristics for the arrival and subsequent recirculation of the contrast agent, the shape of the signal was not modified whatever the treatment. However, CBV seemed to be more sensitive to treatment in the U87 model. This observation supports the concept that rCBV or relative cerebral blood flow may vary in response to anti-angiogenic or chemotherapeutic drugs.[14,43] Notably, VSI was significantly correlated to overall survival and late volumetric determination by MRI in the U251 model. These data underscore the necessity of multiple approaches to identify and discriminate among several microcirculatory parameters vs the simple assessment of blood volume during therapy.[24] A treatment may potentially change vessel diameter but inversely decrease vascular density so that blood volume remains constant to result in a concomitant loss of sensitivity.

Conclusion

In this multimodal imaging study we demonstrate that FLT in conjunction with μPET is the most pertinent of the imaging biomarkers tested to accurately and precociously predict treatment effects as measured by volumetry and survival in 2 models of human gliomas. CBV, as determined by μMRI, correlated to survival in 1 of the tumor models. Our study underlines the importance of using, in addition to anatomical MRI markers, other complementary and ancillary imaging biomarkers based on PET and MRI to determine early response and precisely the specific tumoral response to a given treatment regimen. These data underscore the need to employ combined imaging approaches to better understand the specific effects of various combined treatments. Even if FLT by itself is highly predictive of treatment efficacy, we also show that a combination of imaging biomarkers was better than any one alone. One could point out that combined FLT and CBV imaging could be readily implemented and applied clinically in patients with GBM treated with bevacizumab and TMZ to refine and enlarge the clinical importance and scope of our findings.

Supplementary Material

Supplementary material is available online at Neuro-Oncology (http://neuro-oncology.oxfordjournals.org/).

Funding

This study was funded by the Institut National contre le Cancer (INCa), Roche, the Centre National de la Recherche Scientifique (CNRS), the Ministère de l'Enseignement Supérieur et de la Recherche (MESR), the Université de Caen Basse-Normandie (UCBN), the Conseil Regional de Basse-Normandie (CRBN), the European Union–Fonds Européen de Développement Régional (FEDER), and the Trans Channel Neuroscience Network (TC2N).

Acknowledgment

The authors thank Guerbet SA for providing MRI contrast agents.

Conflict of interest statement. None declared.

References

1. Stupp R, Mason WP, van den Bent MJ, et al. Radiotherapy plus concomitant and adjuvant temozolomide for glioblastoma. *N Engl J Med*. 2005;352:987–996.
2. Desjardins A, Friedman HS. Neuro-oncology: glioblastoma-community adjusts to new standard of care. *Nat Rev Neurol*. 2012;8:244–246.
3. Jain RK, di Tomaso E, Duda DG, Loeffler JS, Sorensen AG, Batchelor TT. Angiogenesis in brain tumours. *Nat Rev Neurosci*. 2007;8:610–622.
4. Miletic H, Niclou SP, Johansson M, Bjerkvig R. Anti-VEGF therapies for malignant glioma: treatment effects and escape mechanisms. *Expert Opin Ther Targets*. 2009;13:455–468.

5. Thompson EM, Frenkel EP, Neuwelt EA. The paradoxical effect of bevacizumab in the therapy of malignant gliomas. *Neurology*. 2011;76:87–93.
6. Mathieu V, De Nève N, Le Mercier M, et al. Combining bevacizumab with temozolomide increases the antitumor efficacy of temozolomide in a human glioblastoma orthotopic xenograft model. *Neoplasia*. 2008;10:1383–1392.
7. Jakobsen JN, Hasselbalch B, Stockhausen M, Lassen U, Poulsen HS. Irinotecan and bevacizumab in recurrent glioblastoma multiforme. *Expert Opin Pharmacother*. 2011;12:825–833.
8. Lai A, Tran A, Nghiemphu PL, et al. Phase II study of bevacizumab plus temozolomide during and after radiation therapy for patients with newly diagnosed glioblastoma multiforme. *J Clin Oncol*. 2011;29:142–148.
9. Pérez-Larraya JG, Lahutte M, Petrirena G, et al. Response assessment in recurrent glioblastoma treated with irinotecan-bevacizumab: comparative analysis of the Macdonald, RECIST, RANO, and RECIST + F criteria. *Neuro Oncol*. 2012;14:665–673.
10. Clarke JL, Chang S. Pseudoprogression and pseudoresponse: challenges in brain tumor imaging. *Curr Neurol Neurosci Rep*. 2009;9:241–246.
11. Pope WB, Young JR, Ellingson BM. Advances in MRI assessment of gliomas and response to anti-VEGF therapy. *Curr Neurol Neurosci Rep*. 2011;11:336–344.
12. Dhermain FG, Hau P, Lanfermann H, Jacobs AH, van den Bent MJ. Advanced MRI and PET imaging for assessment of treatment response in patients with gliomas. *Lancet Neurol*. 2010;9:906–920.
13. Yamasaki F, Sugiyama K, Ohtaki M, et al. Glioblastoma treated with postoperative radio-chemotherapy: prognostic value of apparent diffusion coefficient at MR imaging. *Eur J Radiol*. 2010;73:532–537.
14. Lemasson B, Christen T, Tizon X, et al. Assessment of multiparametric MRI in a human glioma model to monitor cytotoxic and anti-angiogenic drug effects. *NMR Biomed*. 2011;24:473–482.
15. Galbán CJ, Bhojani MS, Lee KC, et al. Evaluation of treatment-associated inflammatory response on diffusion-weighted magnetic resonance imaging and 2-[^{18}F]-fluoro-2-deoxy-D-glucose-positron emission tomography imaging biomarkers. *Clin Cancer Res*. 2010;16:1542–1552.
16. Valable S, Lemasson B, Farion R, et al. Assessment of blood volume, vessel size, and the expression of angiogenic factors in two rat glioma models: a longitudinal *in vivo* and *ex vivo* study. *NMR Biomed*. 2008;21:1043–1056.
17. Lemasson B, Valable S, Farion R, Krainik A, Rémy C, Barbier EL. In vivo imaging of vessel diameter, size, and density: a comparative study between MRI and histology. *Magn Reson Med*. 2012; in press.
18. Wester H. Nuclear imaging probes: from bench to bedside. *Clin Cancer Res*. 2007;13:3470–3481.
19. Jacobs AH, Thomas A, Kracht LW, et al. ^{18}F-fluoro-L-thymidine and ^{11}C-methylmethionine as markers of increased transport and proliferation in brain tumors. *J Nucl Med*. 2005;46:1948–1958.
20. Hutterer M, Nowosielski M, Putzer D, et al. O-(2-^{18}F-fluoroethyl)-L-tyrosine PET predicts failure of antiangiogenic treatment in patients with recurrent high-grade glioma. *J Nucl Med*. 2011;52:856–864.
21. Derlon JM, Chapon F, Noël MH, et al. Non-invasive grading of oligodendrogliomas: correlation between in vivo metabolic pattern and histopathology. *Eur J Nucl Med*. 2000;27:778–787.
22. Desjardins A, Reardon DA, Coan A, et al. Bevacizumab and daily temozolomide for recurrent glioblastoma. *Cancer*. 2011;118:1302–1312.
23. Tixier F, Le Rest CC, Hatt M, et al. Intratumor heterogeneity characterized by textural features on baseline ^{18}F-FDG PET images predicts response to concomitant radiochemotherapy in esophageal cancer. *J Nucl Med*. 2011;52:369–378.
24. Valable S, Eddi D, Constans JM, et al. MRI assessment of hemodynamic effects of an angiopoietin-2 overexpression on a brain tumor model. *Neuro Oncol*. 2009;11:488–502.
25. von Baumgarten LD, Brucker D, Tirniceru AL, et al. Bevacizumab has differential and dose-dependent effects on glioma blood vessels and tumor cells. *Clin Cancer Res*. 2011;17:6192–205.
26. Varallyay CG, Muldoon LL, Gahramanov S, et al. Dynamic MRI using iron oxide nanoparticles to assess early vascular effects of antiangiogenic versus corticosteroid treatment in a glioma model. *J Cereb Blood Flow Metab*. 2009;29:853–860.
27. Valable S, Petit E, Roussel S, et al. Complementary information from magnetic resonance imaging and (^{18})F-fluoromisonidazole positron emission tomography in the assessment of the response to an antiangiogenic treatment in a rat brain tumor model. *Nucl Med Biol*. 2011;38:781–793.
28. Horsthuis K, Nederveen AJ, de Feiter M, Lavini C, Stokkers PCF, Stoker J. Mapping of T1-values and gadolinium-concentrations in MRI as indicator of disease activity in luminal Crohn's disease: a feasibility study. *J Magn Reson Imaging*. 2009;29:488–493.
29. Pope WB, Lai A, Mehta R, et al. Apparent diffusion coefficient histogram analysis stratifies progression-free survival in newly diagnosed bevacizumab-treated glioblastoma. *AJNR Am J Neuroradiol*. 2011;32:882–889.
30. Radaelli E, Ceruti R, Patton V, et al. Immunohistopathological and neuroimaging characterization of murine orthotopic xenograft models of glioblastoma multiforme recapitulating the most salient features of human disease. *Histol Histopathol*. 2009;24:879–891.
31. Vredenburgh JJ, Desjardins A, Reardon DA, et al. The addition of bevacizumab to standard radiation therapy and temozolomide followed by bevacizumab, temozolomide, and irinotecan for newly diagnosed glioblastoma. *Clin Cancer Res*. 2011;17:4119–4124.
32. Sanghera P, Perry J, Sahgal A, et al. Pseudoprogression following chemoradiotherapy for glioblastoma multiforme. *Can J Neurol Sci*. 2010;37:36–42.
33. Carnaghi C, Sclafani F, Basilico V, Doherty M. Response assessment in oncology: limitations of anatomic response criteria in the era of tailored treatments. *Q J Nucl Med Mol Imaging*. 2011;55:589–602.
34. Weller M, Stupp R, Hegi M, Wick W. Individualized targeted therapy for glioblastoma: fact or fiction? *Cancer J*. 2012;18:40–44.
35. Shields AF, Grierson JR, Dohmen BM, et al. Imaging proliferation *in vivo* with [F-18]FLT and positron emission tomography. *Nat Med*. 1998;4:1334–1336.
36. Jensen MM, Erichsen KD, Björkling F, et al. Early detection of response to experimental chemotherapeutic Top216 with [^{18}F]FLT and [^{18}F]FDG PET in human ovary cancer xenografts in mice. *PLoS One*. 2010;5:e12965.
37. Schwarzenberg J, Czernin J, Cloughesy TF, et al. 3′-deoxy-3′-18F-fluorothymidine PET and MRI for early survival predictions in patients with recurrent malignant glioma treated with bevacizumab. *J Nucl Med*. 2012;53:29–36.
38. Spence AM, Muzi M, Link JM, et al. NCI-sponsored trial for the evaluation of safety and preliminary efficacy of 3′-deoxy-3′-[^{18}F]fluorothymidine (FLT) as a marker of proliferation in patients with recurrent gliomas: preliminary efficacy studies. *Mol Imaging Biol*. 2009;11:343–355.

39. Ullrich R, Backes H, Li H, et al. Glioma proliferation as assessed by 3′-fluoro-3′-deoxy-L-thymidine positron emission tomography in patients with newly diagnosed high-grade glioma. *Clin Cancer Res*. 2008;14:2049–2055.
40. Rueger MA, Backes H, Walberer M, et al. Noninvasive imaging of endogenous neural stem cell mobilization in vivo using positron emission tomography. *J Neurosci*. 2010;30:6454–6460.
41. Zhang CC, Yan Z, Li W, et al. [^{18}F]FLT-PET imaging does not always "light up" proliferating tumor cells. *Clin Cancer Res*. 2011;18:1303–1312.
42. Chen W, Delaloye S, Silverman DHS, et al. Predicting treatment response of malignant gliomas to bevacizumab and irinotecan by imaging proliferation with [^{18}F] fluorothymidine positron emission tomography: a pilot study. *J Clin Oncol*. 2007;25:4714–4721.
43. Keunen O, Johansson M, Oudin A, et al. Anti-VEGF treatment reduces blood supply and increases tumor cell invasion in glioblastoma. *Proc Natl Acad Sci USA*. 2011;108:3749–3754.